

Thermal conductivity of carbon nanotubes using nonequilibrium molecular dynamics combined with a machine learning potential

Jia-Hua Liu(刘嘉华), Shuo Cui(崔硕), Feng Guo(郭峰), Yu-Shi Wen(文玉史), Chun-Liang Ji(纪春亮), and Xiao-Chun Wang(王晓春)

Citation: Chin. Phys. B, 2026, 35 (**3**): 036302. DOI: 10.1088/1674-1056/ae3471
http://cpb.iphy.ac.cn; http://iopscience.iop.org/cpb

What follows is a list of articles you may be interested in

Laser power-induced Fermi-level shift in graphene/Al_2O_3 under ambient atmosphere: Toward neutralizing unintentional graphene doping

Jamal Q. M. Almarashi, Mohamed K. Zayed, Hesham Fares, Heba Sukar, Takao Ono, Yasushi Kanai, and Mohamed Almokhtar
Chin. Phys. B, 2025, 34 (**6**): 066302. DOI: 10.1088/1674-1056/adc6f3

Phonon dichroism in proximitized graphene

Wen-Yu Shan(单文语)
Chin. Phys. B, 2023, 32 (**10**): 106301. DOI: 10.1088/1674-1056/acf207

AA-stacked borophene-graphene bilayer as an anode material for alkali-metal ion batteries with a superhigh capacity

Yi-Bo Liang(梁艺博), Zhao Liu(刘钊), Jing Wang(王静), and Ying Liu(刘英)
Chin. Phys. B, 2022, 31 (**11**): 116302. DOI: 10.1088/1674-1056/ac7859

Reduction of interfacial thermal resistance of overlapped graphene by bonding carbon chains

Yuwen Huang(黄钰文), Wentao Feng(冯文韬), Xiaoxiang Yu(余晓翔), Chengcheng Deng(邓程程), and Nuo Yang(杨诺)
Chin. Phys. B, 2020, 29 (**12**): 126303. DOI: 10.1088/1674-1056/abc677

Thermal transport in semiconductor nanostructures, graphene, and related two-dimensional materials

Alexandr I. Cocemasov, Calina I. Isacova, Denis L. Nika
Chin. Phys. B, 2018, 27 (**5**): 056301. DOI: 10.1088/1674-1056/27/5/056301

SPECIAL TOPIC — Heat conduction and its related interdisciplinary areas

Thermal conductivity of carbon nanotubes using nonequilibrium molecular dynamics combined with a machine learning potential

Jia-Hua Liu(刘嘉华)[1], Shuo Cui(崔硕)[1], Feng Guo(郭峰)[1,†], Yu-Shi Wen(文玉史)[2], Chun-Liang Ji(纪春亮)[3], and Xiao-Chun Wang(王晓春)[1]

[1] *School of Physical Science and Information Technology, Liaocheng University, Liaocheng* 252000, *China*
[2] *Institute of Chemical Materials, China Academy of Engineering Physics (CAEP), Mianyang* 621900, *China*
[3] *School of Mechatronical Engineering, Beijing Institute of Technology, Beijing* 100081, *China*

(Received 28 October 2025; revised manuscript received 6 January 2026; accepted manuscript online 7 January 2026)

Large-scale and long-time-span nonequilibrium molecular dynamics simulations have been performed to determine the thermal conductivity of single-walled and double-walled carbon nanotubes (CNTs) using a machine learning potential trained on atomic energies and forces from density functional theory calculations for sp^2-hybridized carbon. The size dependence of graphene and CNTs up to 1 μm has been studied with 200000 atoms and simulation times up to 5 ns. The simulations reveal that thermal transport, whether ballistic, quasi-ballistic, or diffusive, is determined by the relationship between the sample length and the effective mean-free path (MFP). The system size has less effect on thermal conductivity when the sample length significantly exceeds the MFP. Radial tensile strain in CNTs causes the C–C bond length to increase in smaller-diameter CNTs, resulting in a phonon softening effect that subsequently reduces thermal conductivity. An analytical function is proposed to describe the relationship between phonon relaxation time and nanotube diameter. The thermal conductivity of the double-walled CNT is lower than that of an equivalent-size single-walled CNT. Phonon–phonon scattering, interlayer van der Waals interactions, and degenerate coupling of transverse acoustic modes are considered to contribute to the reduction in thermal transport.

Keywords: graphene, carbon nanotube, phonon scattering, lattice thermal conductivity

PACS: 63.20.K–, 82.20.Wt, 63.22.Rc, 51.20.+d

DOI: 10.1088/1674-1056/ae3471 **CSTR:** 32038.14.CPB.ae3471

1. Introduction

Over the past decade, low-dimensional materials[1,2] have attracted substantial research interest, as they can enhance the design and efficiency of various advanced systems.[3] Measuring thermal conductivity (κ) in low-dimensional materials presents significant experimental challenges. These difficulties arise from inherent technical complexities in characterizing suspended nanostructures,[4,5] limited controllability when systematically varying material dimensions, and the lack of standardized protocols for sample quality assessment and measurement techniques. Additionally, different experimental conditions and assumptions used in various measurement methods often lead to inaccurate estimates of thermal conductivity.[6]

Machine learning interatomic potentials (MLIPs)[7] are emerging as new tools to bridge the gap between density functional theory (DFT) and empirical potentials. Recently, significant efforts have been made to construct interatomic potentials using ML models such as artificial neural networks,[8] Behler–Parrinello neural-network potential,[9] spectral neighbor analysis potentials,[10] moment tensor potentials,[11] deep potential,[12] atomic cluster expansion,[13] reactive force field with neural networks (ReaxFF-*nn*),[14] neuroevolution potential,[15] and Gaussian approximation potential (GAP),[16] offering enhanced predictive capability for complex systems. MLIPs have been demonstrated to predict structural, physical, mechanical, chemical, and thermodynamic properties with DFT-level accuracy, while simultaneously reducing computational costs by several orders of magnitude and thereby expanding the spatial and temporal scales of atomic simulations.[17–19] In addition, machine learning can also be employed to construct explicit predictive models for directly estimating the thermal conductivity and other heat transport properties of materials, bypassing explicit and computationally expensive calculations of atomic energies and forces.[20,21]

Graphene and carbon nanotubes (CNTs)[22,23] have become the most popular materials for thermal applications owing to their ultra-high thermal conductivity[24,25] and unique behavior of thermal transport. CNTs are one-dimensional nanomaterials with a hollow tubular structure formed by rolling graphene sheets. Although they exhibit metal-like properties, their thermal transport is predominantly governed by the collective vibration of atoms,[24] i.e., phonons. Su-

†Corresponding author. E-mail: gfeng.alan@foxmail.com

© 2026 Chinese Physical Society and IOP Publishing Ltd. All rights, including for text and data mining, AI training, and similar technologies, are reserved.

per high thermal conductivity of CNTs has been reported (6600 $W \cdot m^{-1} \cdot K^{-1}$)[26] at room temperature. More recently, Li *et al.*[27] reported 1109–1651 $W \cdot m^{-1} \cdot K^{-1}$ for CNTs at 316 K with different diameters measured using Raman spectroscopy, and Zhao *et al.*[28] reported 1512.4 $W \cdot m^{-1} \cdot K^{-1}$ for CNT (16,34) measured using a customized electro-thermal microchip. Furthermore, the thermal conductivity of CNTs is reported to be affected by several factors.[29,30] Hone reported that κ of bundled CNTs is an order of magnitude smaller than that of isolated ones, indicating that phonon–phonon coupling reduces thermal conductivity. Cao *et al.*[31] reported that due to the higher probability of the Umklapp process, CNTs with smaller diameters have higher thermal conductivity. It is generally acknowledged that the thermal conductivity of CNTs is length-dependent owing to their long intrinsic mean-free path (MFP) of phonons.[32] As the length of CNTs increases, phonon transport undergoes ballistic transport when the length is much smaller than the MFP, ballistic-diffusive or quasi-ballistic transport when the length approaches the MFP, and diffusive transport when the length is much larger than the MFP.[33] Whether the superdiffusive phonon transport mechanism exists or the value of κ saturates to an intrinsic value remains controversial.[34]

Based on nonequilibrium molecular dynamics (NEMD) simulations, Maruyama[35] and Zhang and Li[36,37] demonstrated that the thermal conductivity of CNTs exhibits graphene-like power-law scaling behavior with system size. Similar length-dependent trends in the thermal conductivity of single-walled carbon nanotubes (SWCNTs) were also reported by Lukes and Zhong,[38] Lindsay *et al.*,[34] and Bruns *et al.*[39] However, there were significant deviations in the obtained values depending on the empirical potential function or parameter set used. Furthermore, Bruns *et al.*[39] discussed that the tube-length dependence exceeds what MD simulations can reach, as they simulated 10 μm and 10^6 atoms, yet the value of κ still increases following a power-law divergence ($\kappa \sim L^{\alpha}$).

Double-walled CNTs (DWCNTs), composed of two SWCNTs, exhibit richer emerging behavior than SWCNTs owing to quantum coupling. Liu *et al.*[40] found that the radial-breathing mode oscillations are collective modes characterized by concerted inner- and outer-wall motions, and that vibration frequencies can be determined quantitatively from the tube-dependent van der Waals potential. DWCNTs, aligned as two concentric SWCNTs with different twists along their axis, can form Moiré patterns, and vibrational coupling has been observed in the radial breathing mode.[41] In addition, DWCNTs are more than the simple sum of two SWCNTs and can be treated as novel materials. Therefore, more theoretical studies are necessary to unravel these properties.

In this study, we employed NEMD simulations combined with the ReaxFF-*nn* machine learning potential (MLP)[14,42] to investigate the thermal conductivity of carbon-based nanomaterials. First, the size-dependent effects from the perspective of relaxons as the primary heat carriers were analyzed. Second, the spontaneous strain induced by rolling graphene into CNTs was identified, and the influence of this structural transformation on thermal transport was explored. This study examined the thermal conductivity of DWCNTs with van der Waals interactions, focusing on the effects of bond length, phonon density of states, and collective radial vibration on heat conduction.

2. Methodology

2.1. Details of molecular dynamics simulations

This study employed NEMD simulations using the ReaxFF-*nn* potential. All MD simulations were conducted using the Large-scale Atomic/Molecular Massively Parallel Simulator (LAMMPS).[43,44] A time step of 0.1 fs was adopted. The system was first relaxed under NPT and NVT ensembles for 0.5 ns each to fully eliminate internal stress, followed by NVE ensemble simulations of up to 5 ns depending on the system length. The materials studied in this work included single-layer graphene, armchair CNTs ranging from (4,4) to (10,10), DWCNTs with normal interlayer spacing such as (4,4)@(9,9), and DWCNTs with abnormal interlayer spacing such as (6,6)@(9,9) and (5,5)@(9,9). The NEMD simulation setup is illustrated in Fig. 1(a), where the simulation length is denoted as L. Periodic boundary conditions were applied perpendicular to the heat transfer direction, while free boundary conditions were imposed along the heat transfer axis. Fixed layers were positioned at both ends to constrain atomic motion. Previous studies have demonstrated that the Langevin thermostat is more effective and reliable than the Nosé–Hoover chain[45,46] method for local temperature control in NEMD simulations. Consequently, Langevin thermostats were applied to the cold and hot regions to establish heat sinks, with the thermostat length and damping parameter adjusted according to the simulation length.[47] All structural visualizations were rendered using Ovito.[48]

2.2. Thermodynamic property calculations

This study investigated the thermal conductivity of single-layer graphene and various CNTs as a function of length using Fourier's law

$$\kappa = -\frac{J}{\nabla T}, \tag{1}$$

where J represents the heat flux of the material, and the temperature gradient ∇T was extracted by performing piecewise linear regression on the temperature distribution along the transport direction. The calculation of the total heat flux and temperature gradient has been clearly explained in previous

studies.[49–51] In the calculation of the thermal conductivity of graphene, the cross-sectional area A of single-layer graphene was expressed as $A = W \times h$, where W is the width of the graphene sample and h is the van der Waals interaction distance; in this study, $h = 0.34$ nm was adopted.

For SWCNTs, the cross-sectional area A was defined as $A = \pi \cdot h \cdot D$ (i.e., the tube was treated as a cylindrical structure), where D is the nanotube's diameter. The simulation model is shown in Fig. 1(a). Figure 1(b) illustrates the cross-sectional area of DWCNTs, which was divided into three distinct regions: green, yellow, and blue. The green region was defined by extending the outer wall of the DWCNT outward by $0.5h$ (where $h = 0.34$ nm). The yellow region represents the area between the inner and outer walls of DWCNTs. The blue region was defined by extending the inner wall inward by $0.5h$.

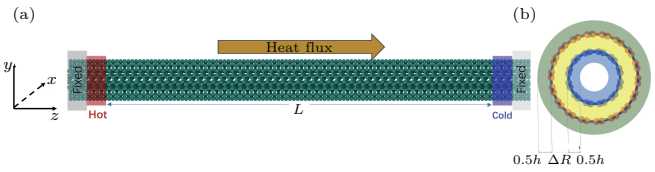


Fig. 1. (a) A schematic illustration of the model used to simulate heat transfer. (b) To calculate the heat flux J, the cross-sectional area A is divided into three regions: green, yellow, and blue. The green region is defined by extending the outer wall of a double-walled carbon nanotube outward by $0.5h$ (where $h = 0.34$ nm), the yellow region represents the area between the cross-sectional circles of the inner and outer walls, and the blue region is defined by extending the inner wall inward by $0.5h$.

The NEMD method requires collecting heat flux and temperature data after the system has reached a steady state for calculating thermal conductivity. Therefore, determining when the system reaches a steady state is crucial. The criteria for determining steady state are detailed in supplementary Figs. S1 and S2, in line with previous reports.[52]

2.3. Phonon calculations

Phonon analysis is widely recognized as an effective approach to understanding thermal conductivity mechanisms. We calculated and analyzed the phonon properties of the simulated materials to gain deeper insights into the fundamental physical mechanisms governing thermal conduction.

First-principles calculations were performed using the SIESTA software.[53] The Phonopy package[54] was used to calculate the phonon dispersion relations, with force constants obtained via the finite displacement method. Prior to these calculations, the structures were optimized using the ReaxFF-*nn* force field. For single-layer graphene, the unit cell was expanded to an $8 \times 8 \times 1$ supercell, and for all CNTs, the unit cell was expanded to $1 \times 1 \times 8$ along the Z direction.

To study anharmonic effects, the Alamode software[55] was employed to calculate the anharmonic properties of phonons in graphene. The lattice thermal conductivity $\kappa_L(T)$ was calculated as

$$\kappa_L^{\alpha\beta}(T) = \frac{1}{NV}\sum_q C_q(T) v_q^{\alpha}(T) v_q^{\beta}(T) \tau_q(T), \tag{2}$$

where α and β denote Cartesian components, q represents all possible phonon states, T is the temperature, N is the number of atoms, V is the unit cell volume, $C_q(T)$ is the mode-specific heat, $v_q^{\alpha}(T)$ is the phonon group velocity along α, and $\tau_q(T)$ is the phonon lifetime. The phonon density of states (DOS) can be computed as

$$D(\omega) = \int_0^{\infty} \left(\frac{\sum_i \langle v_i(t_0) v_i(t_0+\tau) \rangle}{\sum_i \langle v_i(t_0) v_i(t_0) \rangle} \right) \mathrm{e}^{2\pi \mathrm{i} \omega t} \, \mathrm{d}t, \tag{3}$$

where v_i denotes the velocity of atom i, ω is the phonon frequency, angle brackets indicate ensemble averaging, and the term in parentheses corresponds to the normalized velocity autocorrelation function, whose Fourier transform yields the phonon DOS. The equipartition theorem is commonly employed in MD simulations,[38] but it is valid only at temperatures exceeding the Debye temperature.[56] We estimated the quantum correction factor[57] and found its contribution to be minor; therefore, quantum corrections were not applied to the final results. Detailed calculations are provided in supplementary Fig. S3.

2.4. Interatomic interaction potential — ReaxFF-*nn*

ReaxFF, developed by van Duin *et al.*, has been widely applied in MD simulations.[58–60] Diao *et al.*[61] studied the thermal conductivity of graphene and CNTs. However, the original ReaxFF, while suitable for reactive MD simulations, performs poorly in phonon band structure calculations.[61] The ReaxFF force field[62] incorporates bond order (BO) terms to describe dynamic bonding behavior, including bond breaking and formation. BO is derived from empirical functions based on interatomic distances, and a two-step procedure is used to calculate it. In the first step, the uncorrected BO, labeled as BO′, is determined as

$$\mathrm{BO}'_{\sigma,\pi,\pi\pi} = \exp\left[p_{\mathrm{bo}_1,\mathrm{bo}_3,\mathrm{bo}_5} \cdot \left(\frac{r}{r^{\sigma,\pi,\pi\pi}} \right)^{P_{\mathrm{bo}_{2,4,6}}} \right], \tag{4}$$

where $p_{\mathrm{bo}_1,\mathrm{bo}_3,\mathrm{bo}_5}$, $p_{\mathrm{bo}_2,\mathrm{bo}_4,\mathrm{bo}_6}$, and $r^{\sigma,\pi,\pi\pi}$ are adjustable parameters. In the next step, the corrected BO is obtained using Eq. (5), as in the original ReaxFF

$$\mathrm{BO}_{ij} = \mathrm{BO}'_{ij} \cdot f_1(\Delta'_i, \Delta'_j) \cdot f_4(\Delta'_i, \mathrm{BO}'_{ij}) \cdot f_5(\Delta'_j, \mathrm{BO}'_{ij}), \tag{5}$$

where f_1, f_4, and f_5 are empirical functions defined in Ref. [62], and Δ'_i and Δ'_j are the sums of uncorrected BO over all atoms neighboring atom$_i$ and atom$_j$, respectively.

We reformulated the BO correction function using a fully connected neural network,[14] represented by

$$\mathrm{BO}_{ij} = \mathrm{BO}'_{ij} \cdot f_{nn}(\Delta'_i, \mathrm{BO}'_{ij}, \Delta'_j), \tag{6}$$

where f_{nn} is a small neural network taking Δ'_i, Δ'_j, and BO'_{ij} as input.

The total energy expressions of ReaxFF and ReaxFF-*nn* are given in

$$E_{\text{bond}_{ij}}^{\text{ReaxFF}} = D_{\text{e}}^{\sigma} \cdot \text{BO}_{ij}^{\sigma} \cdot \exp[p_{\text{be}_1}(1-\text{BO}_{ij}^{\sigma})^{p_{\text{be}_2}}] - D_{\text{e}}^{\pi} \cdot \text{BO}_{ij}^{\pi} - D_{\text{e}}^{\pi\pi} \cdot \text{BO}_{ij}^{\pi\pi}, \quad (7)$$

$$E_{\text{bond}_{ij}}^{\text{ReaxFF-}nn} = D_{\text{e}}^{\sigma} \cdot f_{nn}(\text{BO}_{ij}^{\sigma}, \text{BO}_{ij}^{\pi}, \text{BO}_{ij}^{\pi\pi}). \quad (8)$$

ReaxFF-*nn* retains the fundamental formalism of ReaxFF but demonstrates significantly enhanced computational performance. The phonon band structures of graphene calculated with ReaxFF-*nn* closely match DFT and other MLPs such as GAP-20 and PACE (in supplementary Fig. S4).

Prior to MD simulations, the ReaxFF-*nn* potential was trained against energies and forces derived from DFT-MD simulations. The corresponding force error metrics are shown in supplementary Figs. S5 and S6. DFT calculations were performed using SIESTA[53] with the Perdew–Burke–Ernzerhof (PBE) exchange–correlation functional and a double-ζ polarized basis set. Training data were generated through three distinct approaches: (i) DFT-MD simulations at varied temperatures and pressures, (ii) atomic structure scaling (e.g., scaling the graphene or CNT supercells), and (iii) configurations sampled from classical MD simulations. In the final step, classical MD simulations were conducted with parameters trained on existing data. To avoid dataset redundancy, structural subsets were systematically sampled from MD trajectories via random selection or extraction of configurations exhibiting anomalous energy or unphysical bond lengths. This process was repeated until the interatomic potential met the target performance criteria, using our I-ReaxFF[63] package.

2.5. Phonon spectra

Phonon spectra are highly sensitive to interatomic potential parameters, making them critical benchmarks for accuracy. Phonon dispersion relations offer a convenient means of validation, as they can be directly compared with first-principles calculations and experimental measurements. To evaluate the accuracy of our potential in describing phonon dispersion, we computed the phonon spectrum across the entire first Brillouin zone of graphene. The phonon dispersion relations obtained are shown in Fig. 2.

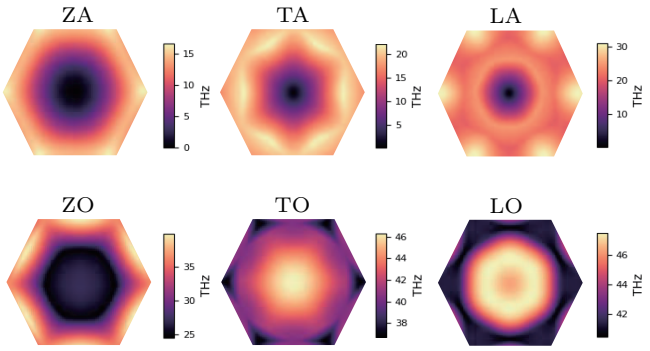


Fig. 2. Phonon dispersion curves for the six branches of graphene within the hexagonal two-dimensional Brillouin zone.

The Brillouin zone of a CNT was constructed by folding the graphene zone, as shown in supplementary Fig. S7. The allowed wavevectors are detailed in the supplementary information. Figures 3(a)–3(d) show the phonon dispersion relations of CNT (5,5) calculated using the Phonopy tool[54] with the AIREBO, GAP-20, Opti-Tersoff, and ReaxFF-*nn* potentials, respectively. Figure 3(e) presents the results obtained from force constants extracted via first-principles calculations using SIESTA.

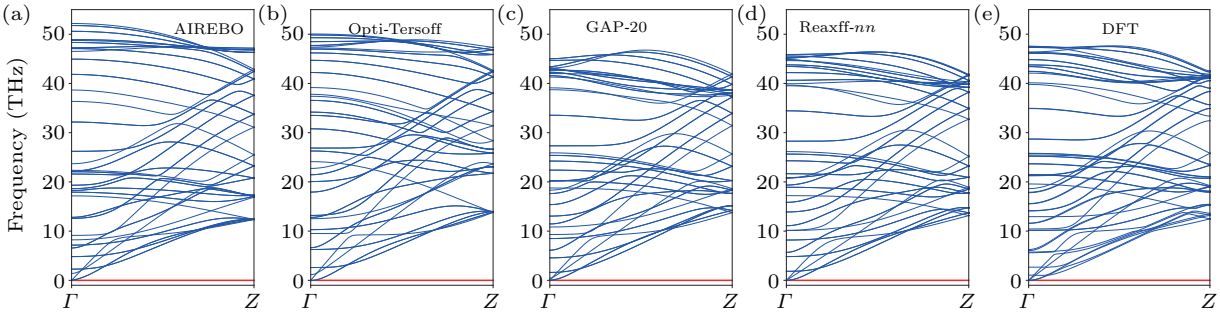


Fig. 3. (a)–(d) Phonon dispersion curves of CNT (5,5) obtained from force constants calculated using the AIREBO, GAP-20, Opti-Tersoff, and ReaxFF-*nn* interatomic potentials, respectively. (e) Phonon dispersion curves from DFT calculations using the SIESTA package with the PBE functional and a double-ζ basis set.

Compared to empirical potentials such as AIREBO[64] and Opti-Tersoff,[65] GAP-20,[66] and ReaxFF-*nn* exhibit better agreement with the DFT-calculated phonon dispersion for the lower-frequency modes, particularly providing more accurate fitting near the upper limit of the optical branches. The phonon density of states of a (5,5) carbon nanotube, computed with the Opti-Tersoff potential, our ReaxFF-*nn* potential, and DFT, is compared in supplementary Fig. S8.

2.6. Thermal conductivity calculations

Thermal conductivity of graphene was calculated using two primary approaches: (i) solving the Boltzmann transport equation (BTE) with higher-order force constants, and (ii) applying the NEMD method according to Fourier's law. Fig-

ure 4(a) compares the thermal conductivity of samples with varying lengths, presenting NEMD simulation results alongside BTE calculations using higher-order force constants computed from different interatomic potentials. For clearer trend comparison, all data were normalized to the thermal conductivity value of a reference sample with length $L = 853$ nm.

Additionally, lattice thermal conductivity was calculated using the ALAMODE[55] code with a q-mesh of $64 \times 64 \times 1$. The comparison reveals that ReaxFF-*nn* and GAP-20 exhibit good agreement with the thermal conductivity predicted by the NEMD method in the range 0–200 nm. This consistency arises because the relaxation time approximation (RTA) treats Normal (N) scattering as a purely resistive mechanism. At small length scales, phonon transport is primarily ballistic, exhibits only weak phonon–phonon coupling, and thus has minimal impact on thermal conductivity.

Figure 4(b) illustrates the cumulative contributions of phonons to the total thermal conductivity across different frequencies, calculated using the AIREBO, Opti-Tersoff, GAP-20, and ReaxFF-*nn* interatomic potentials. The AIREBO potential shows the largest deviation compared to the other three potentials, and previous studies have reported that thermal conductivity predictions using AIREBO are generally lower than those using the Opti-Tersoff potential. At around 10 THz, cumulative thermal conductivity contributes approximately 50% for the AIREBO potential, whereas for the other potentials it is only about 25%–35%. This difference is attributed to the underestimation of phonon contributions by the AIREBO potential in the 10–20 THz frequency range, resulting in an overall lower thermal conductivity prediction. Conversely, the results of all potentials exhibit cumulative thermal conductivity contributions of about 80% around 20 THz, highlighting that low-frequency phonons dominate heat transport.

Optical phonon modes with frequencies above 20 THz contribute little to the total thermal conductivity, and modes above 30 THz contribute almost no direct heat flux. However, these high-frequency modes participate in Umklapp scattering processes, indirectly affecting the magnitude of thermal conductivity.

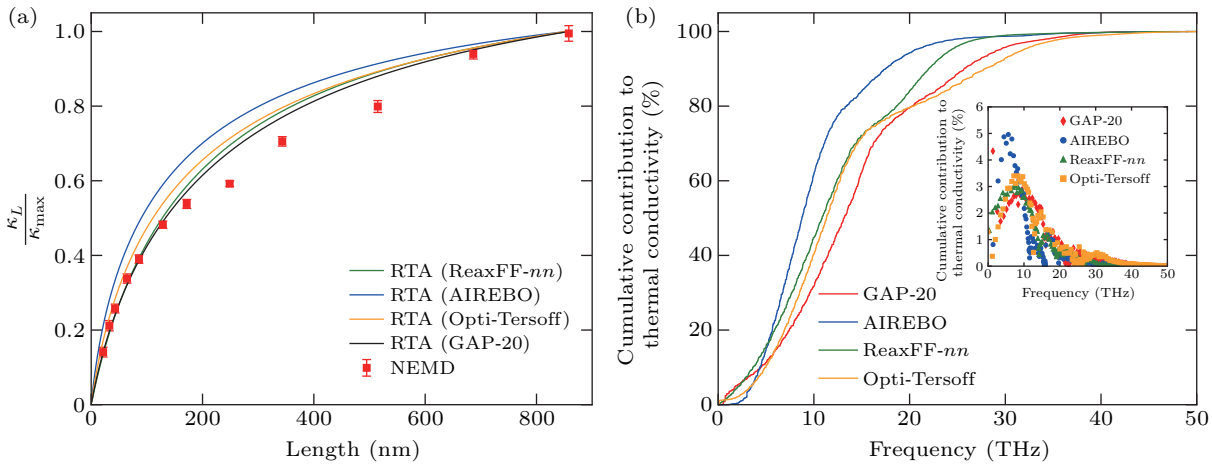


Fig. 4. (a) Thermal conductivity (κ_L) as a function of graphene sample length L. Red squares represent NEMD results obtained using the ReaxFF-*nn* potential, while green, blue, yellow, and black curves correspond to RTA calculations with ReaxFF-*nn*, AIREBO, Opti-Tersoff, and GAP-20 interatomic potentials, respectively. All thermal conductivity values are normalized by $\kappa_{\max}$, corresponding to the value at $L_c = 853$ nm. (b) Comparison of normalized cumulative phonon contributions computed with different interatomic potentials. The corresponding thermal conductivity contribution per unit frequency is plotted as a function of frequency in the inset.

3. Results and discussion

3.1. Size effect

Unlike bulk materials, the thermal conductivity of low-dimensional materials exhibits strong size dependence, a phenomenon known as the size effect.[67] This dependence originates from enhanced phonon–boundary scattering in confined geometries. Previous studies have demonstrated that as the length of a graphene sample increases, phonon transport transitions from ballistic to quasi-ballistic and ultimately to diffusive.[68,69] Specifically, transport is ballistic when the sample length is significantly shorter than the average phonon MFP,[70] quasi-ballistic when the length is comparable to the average MFP, and diffusive when the length substantially exceeds the average MFP. These distinct transport regimes give rise to different trends in thermal conductivity.

Inspired by the novel heat transport theory of relaxons proposed by Cepellotti *et al.*,[71] we extended our analysis of thermal conductivity, which has traditionally been based on phonon properties, to a relaxon-based perspective using MD simulation results. Lattice heat transport under out-of-equilibrium conditions cannot be fully described by the properties of individual phonons, since scattering processes strongly couple phonons with different wave vectors and branches.[72] A relaxon is a collective excitation composed of linear combinations of nonequilibrium phonon populations. In contrast to phonons, different relaxons are mutually decoupled and do not scatter with each other. As a re-

sult, relaxons exhibit longer relaxation times in heat transport. Their propagation velocity approximately represents the speed of heat propagation, and their MFPs are shorter than those of phonons. Moreover, while phonons are quanta of vibrational energy, relaxons act as the true carriers of heat.

Previous studies[24] have shown that when the length of graphene is shorter than the average phonon MFP, heat transport is dominated by ballistic conduction, and the thermal conductivity scales linearly with the sample length (L). In the quasi-ballistic regime, thermal conductivity follows a power-law relationship with length, expressed as $\kappa \propto L^n$ ($0 < n < 1$).[73]

Thermal conductivity of a finite-length sample can be expressed using the phonon–boundary scattering model as

$$\kappa(L)^{-1} = \kappa_\infty^{-1}\,(1+\lambda/L)\,, \tag{9}$$

where $\kappa(L)$ is the thermal conductivity of a sample of length L, κ_∞ is the intrinsic (diffusive limit) thermal conductivity of an infinitely long sample, and λ represents the average phonon MFP.[61]

As shown by the data points in Fig. 5(a), the thermal conductivity of graphene increases linearly with sample lengths from 21.4 nm to 85.3 nm. From the phonon transport perspective, this range corresponds to ballistic transport, where the sample size is smaller than the average phonon MFP.[74] However, by fitting the quasi-ballistic transport region of graphene (approximately between 245 nm and 853 nm) using Eq. (9), we obtained an average phonon MFP of 415.3 nm and a thermal conductivity of 2045.84 $\mathrm{W\cdot m^{-1}\cdot K^{-1}}$ in the diffusive limit.

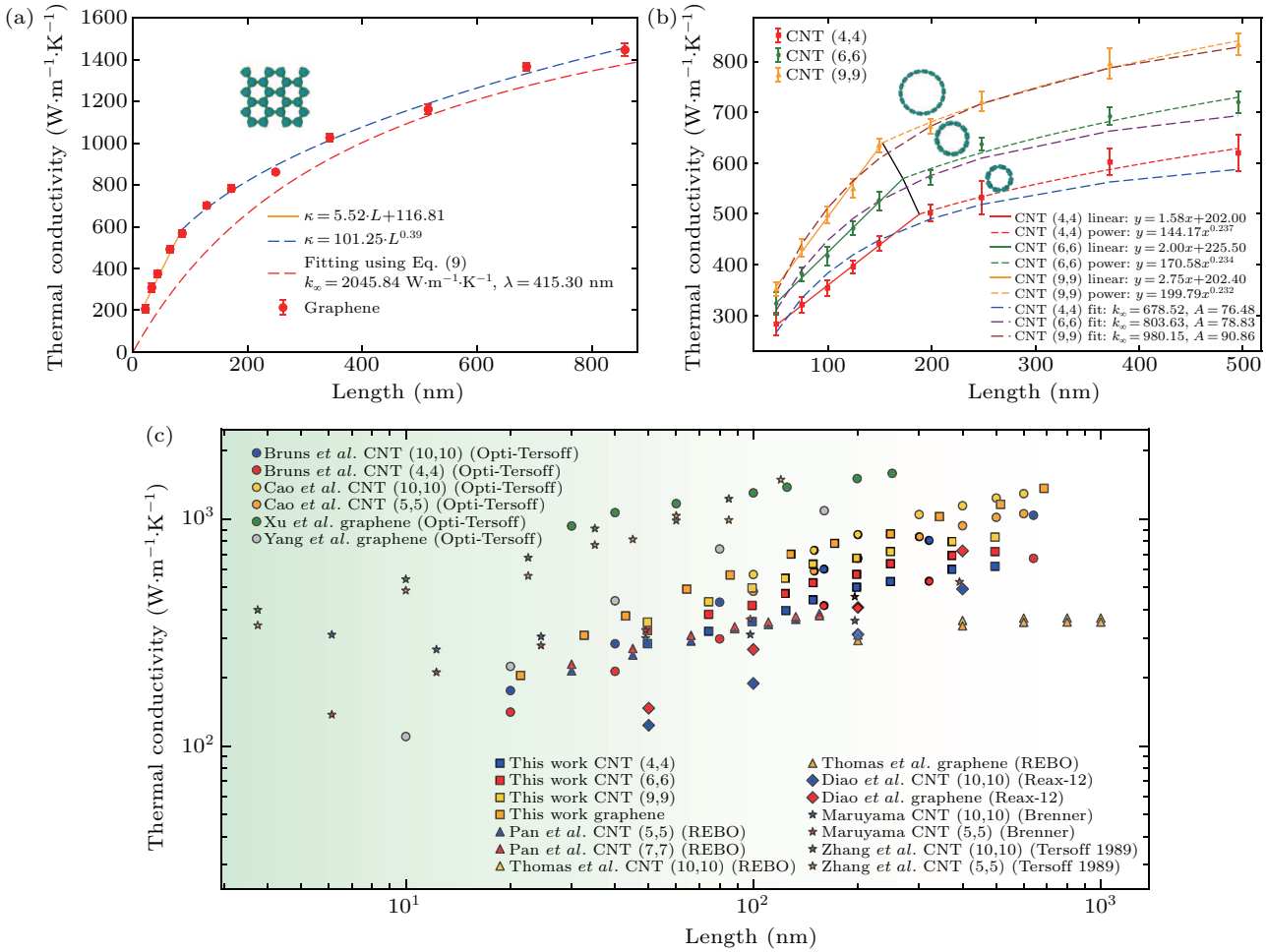


Fig. 5. Thermal conductivity as a function of system size. (a) Computed thermal conductivity of graphene, fitted using Eq. (9) and the power-law relation $\kappa \propto L^n$ ($n = 0.39$ for graphene, $n = 0.24$ for CNT (4,4), $n = 0.23$ for CNT (6,6), and $n = 0.23$ for CNT (9,9)), respectively. (b) Computed thermal conductivity of CNT (4,4), CNT (6,6), and CNT (9,9), fitted using Eq. (9) and the power-law relation, respectively. The black line connects the intersection points of the linear and power-law fits. (c) NEMD data for the thermal conductivity of isolated nanotubes at room temperature for different sizes and potential models. Reference data are from Maruyama,[35] Zhang and Li,[36] Bruns *et al.*,[39] Diao *et al.*,[61] Wang *et al.*,[68] Cao and Qu,[73] Xu *et al.*,[74] Thomas *et al.*,[75] and Pan *et al.*[76]

These several-fold differences observed between the two calculation approaches prompted us to reflect on the definition and theoretical framework of relaxons. From the perspective of relaxons as heat carriers, we examined the time required for graphene to reach thermal steady state[77] (i.e., when the temperature gradient no longer increases with simulation time) at various sample lengths. As shown in supplementary Fig. S2, this time exhibits an approximately linear relationship within

the specified size range. Therefore, we considered the intersection point between the linear fit and power-law fit as the average MFP of relaxons, while the MFP obtained from fitting Eq. (9) corresponds to phonons with a larger theoretical average MFP (the fitting results are shown in Table 1).

Diao *et al.*[61] calculated the size effect on the thermal conductivity of graphene using three different ReaxFF potentials and found that the thermal conductivity in the diffusive limit ranged from 759.6 $\mathrm{W\cdot m^{-1}\cdot K^{-1}}$ to 1393.1 $\mathrm{W\cdot m^{-1}\cdot K^{-1}}$. Using the ReaxFF-*nn* potential, we predicted a thermal conductivity of 2045.84 $\mathrm{W\cdot m^{-1}\cdot K^{-1}}$. Table 2 lists previously reported experimental data for graphene and CNTs, which are compared with our computational results. Our predicted value is in good agreement with the experimental data of Xu *et al.*[74] (1689–1813 $\mathrm{W\cdot m^{-1}\cdot K^{-1}}$) and Cai *et al.*[78] (2500 $\mathrm{W\cdot m^{-1}\cdot K^{-1}}$). The fitted phonon relaxation MFP of 415.3 nm is consistent with the results of previous studies (300–600 nm).[69]

Maruyama[35] and Zhang and Li[36] demonstrated that the thermal conductivity of CNTs also exhibits graphene-like power-law scaling behavior with system size. The κ of CNT (5,5) and (10,10) has been fitted by a power-law relation $\kappa \propto L^n$ $(0 < n < 1)$, with an exponent of $n = 0.32$ obtained for CNT (5,5) and an almost length-independent behavior for CNT (10,10).[35] Zhang and Li[36] performed a similar analysis for CNT (5,5) and CNT (10,10), yielding exponents of $n = 0.40$ and $n = 0.36$, respectively. Savin *et al.*[79] also calculated the thermal conductivity of CNTs with three different diameters and analyzed the size dependence using a power-law fitting approach. In addition, Cao and Xu[73] investigated the size dependence of thermal conductivity in graphene and CNTs with different diameters and found that the data for all systems could be described by the same scaling relation, yielding a common exponent of $n = 0.21$.

Different from the aforementioned results, as shown in Fig. 5(b), when fitting our data using the same scaling relation, a distinct trend is observed. For graphene, the fitted exponent is $n = 0.39$, whereas for CNTs with various diameters, n is approximately 0.23, showing a slight decrease as the diameter increases.

Notably, the power-law exponent obtained for CNTs in this work is smaller than those reported by Maruyama[35] and Zhang and Li[36] We attribute this discrepancy primarily to the different fitting procedure and fitting range. Linear fitting is applied for CNTs at smaller lengths, while longer CNTs are fitted with the power-law formula, following a methodology similar to that adopted by Cao and Xu[73] Additionally, the use of different interatomic potential models may contribute to this difference, as discussed in the previous section regarding variations in phonon spectra.

The thermal conductivity from simulations[35,36] with Tersoff 1989[80] and Brenner[81] potential for CNT (5,5) exceeds that of CNT (10,10), whereas the Opti-Tersoff potential gives a different conclusion,[39,73] showing that the thermal conductivity of CNT (5,5) remains lower than that of CNT (10,10) up to a length of approximately 2400 nm. Considering that the Opti-Tersoff and ReaxFF-*nn* potentials give better performance on phonon structures and force calculations, the corresponding thermal conductivity calculations are more reliable.[82] Interestingly, Bruns's[39] study revealed that at much larger lengths (exceeding 5 μm), the thermal conductivity of CNT (4,4) increases more rapidly than that of CNT (10,10). Experimental findings by Zhao *et al.*[28] demonstrate that the thermal conductivity of CNTs increases monotonically with diameter, a trend consistently captured in our and Cao's NEMD simulations[73] within the accessible length range.

As shown in Fig. 5(c), thermal conductivity values obtained using the ReaxFF-*nn* potential are generally higher than those obtained with the Brenner potential,[81] the REBO potential (Brenner II),[75,76] and the traditional ReaxFF potential,[61,83] but lower than those predicted by the Opti-Tersoff potential[68,74] and Tersoff 1989 potential.[80] To facilitate a direct comparison with other reported values, results from Zhang and Li,[36] which originally employed a cross-sectional thickness of 1.44 Å, were re-calibrated using a standard thickness of 3.4 Å. Regarding the size effect, thermal conductivity calculated using the REBO potential converges when the size is below 1 μm, while the traditional ReaxFF potential shows a relatively uniform growth rate on a logarithmic scale, without exhibiting any convergence trend within the calculated range.

Strikingly, thermal conductivity predicted by REBO potentials decreases with increasing diameter, and the predicted thermal conductivity of graphene is lower than that of CNTs, which is distinct from most theoretical results. Drawing on the study by Si *et al.*,[82] this discrepancy can be attributed to the underestimation of the frequency range and high-frequency peak of the ZA and ZO modes inherent in the REBO and AIREBO potentials. This localized vibrational deficiency leads to a substantial underestimation of thermal conductivity in larger-diameter CNTs and graphene, where these out-of-plane modes play a dominant role in heat transport.

Using the fitting in Eq. (9), the phonon average MFP for the three CNTs was obtained as 76.48 nm, 78.93 nm, and 90.06 nm, which are in close agreement with the 100 nm value calculated by Hone *et al.*[84] The fitted diffusive thermal conductivity of CNT (9,9) is 980.15 $\mathrm{W\cdot m^{-1}\cdot K^{-1}}$. From Table 2 and Figs. 5(b) and 5(c), it is observed that this value is closer to the thermal conductivity measured by Kazuki Yoshino for CNT (9,8) $(1166 \pm 243\ \mathrm{W\cdot m^{-1}\cdot K^{-1}})$[85] and by Feng *et al.*[86] for CNTs with a diameter of 1.88 nm (1439 $\mathrm{W\cdot m^{-1}\cdot K^{-1}}$) compared to other potentials. Although

experimental measurements for CNT (4,4) and CNT (6,6) are limited, our results are in good agreement with previous computational results obtained using the NEMD method, as shown in Fig. 5(c). Based on the intersection point of the power-law and linear fits, the average MFP of relaxons for CNT (4,4), CNT (6,6), and CNT (9,9) is 187 nm, 171 nm, and 152 nm, respectively, whereas the relaxon MFP for graphene is 84.61 nm.

As shown in Table 1, the size effects of graphene and CNTs with different diameters from both the relaxon and phonon perspectives are studied using two fitting methods. This analysis reveals a distinct trend: the average MFP of relaxons (λ_{relaxon}) monotonically decreases from smaller-diameter CNTs to graphene. In contrast, the average phonon MFP (λ_{phonon}), obtained from fitting Eq. (9), exhibits an opposite trend.

Table 1. The extrapolated average phonon MFP, relaxon MFP, and diffusive thermal conductivity of graphene and CNTs.

Sample	κ_∞ ($\text{W}\cdot\text{m}^{-1}\cdot\text{K}^{-1}$)	λ_{phonon} (nm)	λ_{relaxon} (nm)
CNT (4,4)	678.52	76.48	187.68
CNT (6,6)	803.63	78.83	171.95
CNT (9,9)	980.15	90.86	152.25
Graphene	2045.84	415.30	84.61

Table 2. Previously reported values on thermal conductivity of graphene and CNTs near room temperature. Here, '∼' indicates an unknown size.

Diameter (nm)	Size (μm)	κ ($\text{W}\cdot\text{m}^{-1}\cdot\text{K}^{-1}$)	Refs.
1.15	10–12	1166	[85]
1.36	25	1651	[91]
1.7	2.6	3300	[92]
1.8	41	2400	[93]
1.88	10	1439	[86]
2.4	2	3600	[94]
2.59	∼	1981.2	[28]
3	2.76	2000	[95]
Graphene	∼	2500	[78]
Graphene	9	1689–1813	[74]

This result is consistent with the findings of Zhou *et al.*,[87] where CNTs exhibit longer carrier lifetimes compared to graphene due to reduced scattering. Consequently, relaxons are recognized as the primary heat carriers, and their lifetimes increase progressively from graphene to smaller-diameter CNTs, assuming the sound velocity remains unchanged. This observation aligns with the conclusions of Jensen *et al.*[88] and Liang *et al.*[89] that rolling two-dimensional materials into nanotubes extends carrier lifetimes.

Radial vibrations increase with nanotube diameter. In smaller-diameter CNTs, out-of-plane vibrational modes are strongly suppressed by high curvature and spatial confinement. As the structure approaches the planar geometry of graphene, these out-of-plane radial vibrations are enhanced. With increasing tube diameter, these modes partially evolve into flexural ZA branches, which are the dominant contributors to the thermal conductivity of graphene.[73,90] This evolution effectively compensates for the reduction in carrier lifetime, resulting in higher thermal conductivity in larger-diameter CNTs. Hence, while longer carrier lifetimes in small-diameter CNTs are beneficial, the restricted vibrational spectrum limits its overall heat transport. Conversely, the enhanced radial vibrational contributions in larger-diameter CNTs substantially improve thermal conductivity, achieving superior heat conduction performance.

3.2. Diameter-dependent thermal conductivity in CNTs

By comparing armchair SWCNTs of different diameters at a fixed length, we found that their thermal conductivity is lower than that of monolayer graphene at the same length. However, as the diameter increases, the thermal conductivity gradually approaches that of graphene. Notably, recent experiments[28] indicate that the rate of increase slows for larger-diameter nanotubes.

This trend can be attributed to two main factors. First, phonon DOS analysis shows that increasing the diameter induces a blue shift in high-frequency modes and a red shift in low-frequency modes, reflecting a phonon hardening effect as reported by Kodama *et al.*,[96] Parrish *et al.*,[97]

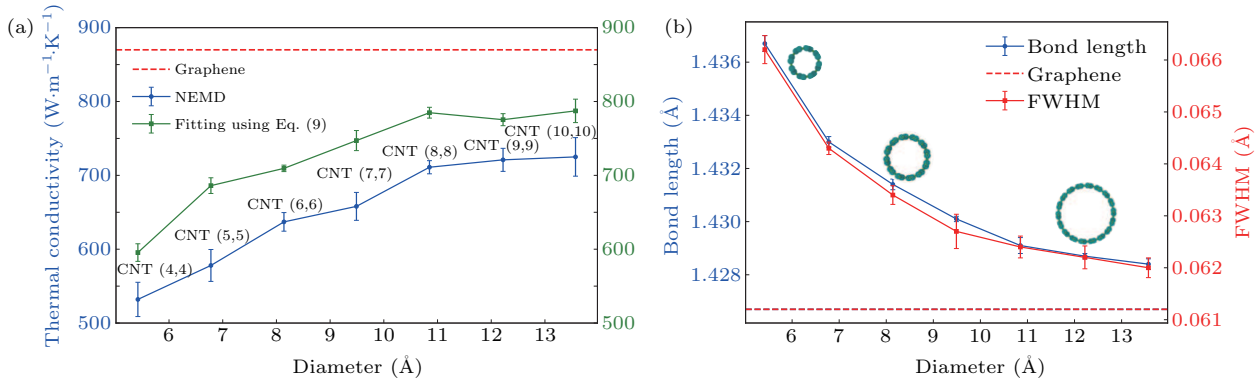


Fig. 6. (a) Thermal conductivity of SWCNTs as a function of tube diameter. Blue points represent NEMD simulation results, green points correspond to fitted values using Eqs. (10) and (11), and the red horizontal line denotes the thermal conductivity of graphene. (b) Variation of bond length and radial distribution function (RDF) full width at half maximum (FWHM) with SWCNT diameter. Blue points indicate average bond lengths, red points denote RDF FWHM values, and red horizontal lines show the corresponding bond length and FWHM values for graphene.

and Xiao and Yuan[98] These frequency shifts reduce Umklapp scattering probability, thereby enhancing thermal conductivity in larger-diameter CNTs. Second, changes in phonon relaxation time play a role. Increased curvature reduces the phonon relaxation time,[99] which can be qualitatively captured by $\tau = (1 - 0.5h/D)$, where τ denotes the phonon relaxation time, h is the effective graphene thickness (0.34 nm), and D is the nanotube diameter.

The thermal conductivity of CNTs is fitted using

$$\kappa_{\text{fit}} = \kappa_{\text{g}} \frac{G(\text{cum})_{\text{cnt}}}{G(\text{cum})_{\text{g}}} \left(1 - \frac{0.5h}{D}\right), \tag{10}$$

where κ_{g} is the thermal conductivity of graphene obtained from NEMD simulations, $G(\text{cum})_{\text{cnt}}$ and $G(\text{cum})_{\text{g}}$ are the cumulative phonon DOS of CNTs and graphene up to cum THz, D is the CNT diameter, and $h = 0.34$ nm. The cumulative DOS up to a cutoff frequency cum is defined as

$$G(\text{cum}) = \frac{\int_0^{\text{cum THz}} \text{dos}(\omega)\, \text{d}\omega}{\int_0^{\infty} \text{dos}(\omega)\, \text{d}\omega}, \tag{11}$$

where $\text{dos}(\omega)$ denotes the phonon density of states at frequency ω.

Previous studies[24] have reported that phonons responsible for heat transport predominantly reside in the low-frequency region (100 GHz to 10 THz). Based on the computational results shown in Fig. 4(b), we therefore selected 20 THz as the cutoff frequency for cumulative contributions. Using Eqs. (10) and (11), the thermal conductivity of CNTs with different diameters was fitted and compared with our NEMD simulation results. The fitting outcomes and their comparison with NEMD data are presented in Fig. 6(a). Furthermore, compared to graphene, the curvature of CNTs modifies C–C bond lengths, which can be quantitatively analyzed via the radial distribution function (RDF).[100] This aspect is further discussed in the following sections.

3.3. Phonon density of states

Figure 7 shows the low-frequency phonon density of states (DOS) for CNTs ranging from SWCNT(7,7) to SWCNT(10,10). As the CNT diameter increases, the peak in the radial phonon DOS associated with the radial breathing mode shifts to lower frequencies. Specifically, the first low-frequency peak moves from 2.45 THz in SWCNT(4,4) to 0.64 THz in SWCNT(10,10). Since monolayer graphene lacks a pronounced peak in this low-frequency range, no direct comparison is provided. The nonzero intensity near 0 THz arises from the fixed boundary conditions applied at both ends.[38]

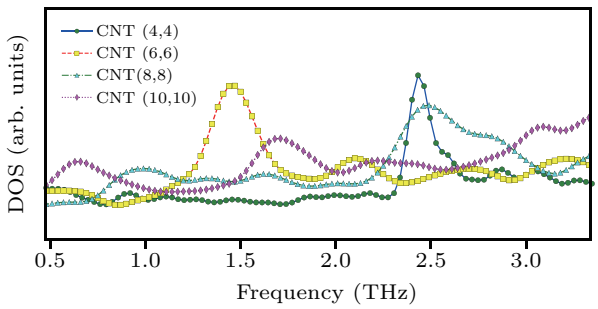


Fig. 7. Radial phonon DOS shifts of SWCNTs with chiralities (4, 4), (6, 6), (8, 8), and (10, 10).

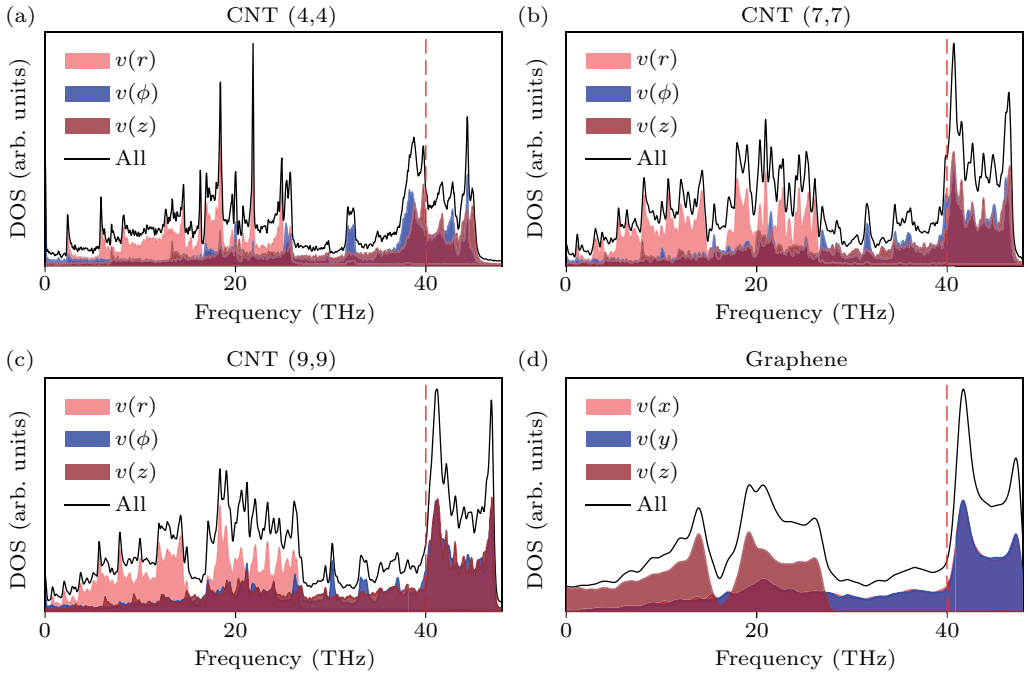


Fig. 8. Total phonon DOS and its directional components for (a) CNT (4, 4), (b) CNT (7, 7), (c) CNT (9, 9), and (d) graphene, respectively. For CNTs, the phonon DOS is decomposed in cylindrical coordinates into radial (r), tangential (ϕ), and axial (z) vibrations. For graphene, the phonon DOS is decomposed in Cartesian coordinates into x, y, and z directions. The red vertical line at 40 THz indicates the phonon frequency blue shift.

In contrast, high-frequency peaks in the total phonon DOS shift toward higher frequencies with increasing diameter, as illustrated in Fig. 8. Here, the red line indicates the progression of peaks from below 40 THz to above 40 THz. A decomposition of the vibrational modes (Fig. 8) shows that the radial vibrations of carbon atoms in CNTs correspond to out-of-plane (Z-direction) vibrations in graphene, whereas tangential and axial vibrations map to in-plane (X and Y directions) vibrations. Details of velocity component calculations are provided in supplementary Fig. S9.

Radial, or out-of-plane, vibrations dominate the low-frequency phonon DOS, and the first PDOS peak near 1 THz shifts to lower frequencies as the tube diameter increases. Previous studies have shown that this component is highly sensitive to the nanotube diameter.[73] Conversely, the difference between tangential and axial phonon DOS decreases with increasing diameter, approaching the graphene limit, which is a consequence of reduced curvature leading to near equivalence of tangential and axial vibrations.

The observed red shift of low-frequency phonon DOS peaks is primarily attributed to phonon hardening. As the CNT diameter increases, the acoustic branches shift to lower frequencies, which reduces phonon scattering rates.[101] Simultaneously, high-frequency optical branches exhibit a blue shift, suppressing Umklapp scattering. The combined effect of prolonged acoustic phonon lifetimes and diminished Umklapp scattering with increasing diameter contributes to the enhanced thermal conductivity of larger-diameter CNTs.

3.4. Bond length analysis

Bond length was characterized by RDF. RDF can be expressed as

$$g(r) = \frac{1}{\rho_0} \cdot \frac{\Delta N(r)}{4\pi r^2 \Delta r}, \tag{12}$$

where ρ_0 is the average number density of atoms, $\Delta N(r)$ is the number of atoms located within a spherical shell of thickness Δr at a distance r from a reference atom, and $4\pi r^2 \Delta r$ is the volume of the shell.

Analysis of RDFs for CNTs with different diameters using Eq. (12) reveals that, as the CNT diameter increases, the position of the first peak, which represents the nearest-neighbor bond length, gradually shifts to a lower value, as shown in supplementary Fig. S10. This indicates that bond lengths vary with diameter. A study by Zhang and Zuo[102] has shown that when graphene is rolled into a nanotube, the original uniform bond length of 1.421 Å in graphene splits into two distinct values, d_1 and d_2, in armchair nanotubes. However, only one peak corresponding to the bond length could be identified in the RDF analysis owing to thermal fluctuations.

The full width at half maximum (FWHM) of the RDF peak reflects crystal stiffness. Figure 6(b) demonstrates that increasing the nanotube diameter leads to a gradual reduction in both the C–C bond length and the corresponding FWHM, suggesting enhanced structural stability. A narrower peak signifies higher stiffness, which promotes harmonic vibrations and reduces phonon scattering. Consequently, this leads to enhanced thermal conductivity.[61] These findings align with thermal conductivity measurements under high pressure reported by Zhou *et al.*[103] In contrast, as the tube diameter decreases, the RDF peak broadens relative to that of graphene, indicating a reduction in stiffness. This increased anharmonicity enhances phonon scattering, thereby lowering thermal conductivity in smaller-diameter nanotubes. Analysis of phonon DOS revealed a trend analogous to that observed in studies of strained graphene by Kumar *et al.*,[104] where tensile strain shifts phonon modes toward intermediate frequencies.[105] This suggests that the process of rolling graphene into a nanotube introduces tensile strains, particularly pronounced in smaller-diameter tubes. As evidenced by the shift in phonon DOS toward intermediate frequencies, this strain contributes to a reduction in thermal conductivity. Bond length shows the most notable change between CNT (4,4) and CNT (5,5), after which the rate of change decreases. With an increase in nanotube diameter, both metrics steadily align with graphene values.

Changes in bond length typically have a strong impact on the atomic vibrational amplitude relative to their equilibrium positions. This effect is observed in the significant suppression of out-of-plane vibrations in graphene under tensile strain.[104] In CNTs, radial vibrations generally contribute more to thermal conductivity than vibrations in other directions. Therefore, in this work, we analyzed the material's deviation from equilibrium positions by calculating vibrational intensity, especially radial vibration intensity. The summation method is similar to that used in spectral energy density analysis,[106] and the calculation can be expressed as

$$\mathrm{RBA} = \left\langle \left(\left\| \frac{1}{N \cdot B} \sum_{b=1}^{B} \sum_{n=1}^{N} [r(n,b,t) - r_0(b)]^2 \right\| \right)^{\frac{1}{2}} \right\rangle_t, \tag{13}$$

where N denotes the total number of unit cells, B is the number of atoms per unit cell, and b represents the atom index within each unit cell. The term $r(n,b,t)$ indicates the instantaneous radial distance of atom b in unit cell n from the tube center at time t, while $r_0(b)$ denotes the time-averaged radial distance of atom b from the center over the entire simulation. The angle brackets $\langle \cdot \rangle_t$ indicate averaging over the simulation time. We refer to this quantity as the radial breathing amplitude (RBA). The magnitude of RBA corresponds to the intensity of radial vibrations. As shown in Fig. 9, RBA increases as the CNT bond length decreases, indicating that heat is transferred more efficiently through vibrational modes. This is manifested by

the increase in thermal conductivity with increasing nanotube diameter.

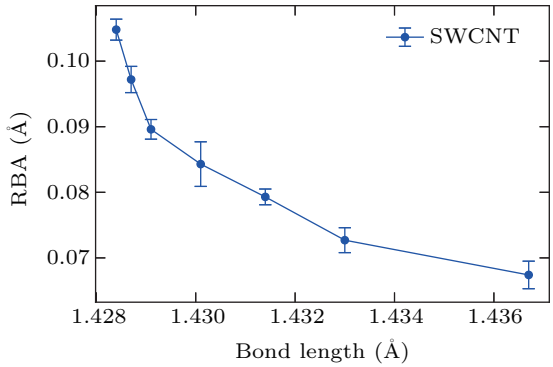


Fig. 9. Relationship between the radial breathing amplitude of SWCNTs and its diameter.

3.5. DWCNTs

Kodama *et al.*[96] obtained the thermal conductivity of the outer wall of DWCNTs by expanding the inner diameter of DWCNTs with an equilibrium interlayer spacing, thereby reducing the interlayer distance and inducing deformation in the outer wall. The minimum interlayer spacing achieved in their study was less than 2.6 Å. Meanwhile, Zhang *et al.*[107] constructed DWCNTs with interlayer distances smaller than the equilibrium spacing — down to the minimum configuration of (7,7)@(10,10) — and calculated their mechanical properties.

In this work, we calculated the overall thermal conductivity of DWCNTs with different interlayer spacings, including contributions from both the inner and outer walls. Figure 10 reveals significant deviations in bond lengths between DWCNTs and their corresponding isolated SWCNTs. Among the configurations studied, the DWCNT (5,5)@(9,9) showed the smallest change, approximately 20 femtometers (fm) for both inner and outer walls, and achieved the highest thermal conductivity. In contrast, the DWCNT (4,4)@(9,9) exhibited a contraction of 120 fm in the inner wall and an expansion of 50 fm in the outer wall. The most pronounced bond length alterations occurred in the DWCNT (6,6)@(9,9), with an inner wall contraction of 2100 fm and an outer wall expansion of 2250 fm, resulting in the lowest thermal conductivity. These variations can be attributed to excessive inter-wall strain. This strain significantly reduces phonon transport efficiency, causing the thermal conductivities of all multi-walled nanotubes to fall below that of the outer tube of the corresponding CNT (9,9).[108]

As shown in supplementary Figs. S11 and S12, the strong radial strain in DWCNT (6,6)@(9,9) resulted in the most pronounced difference in phonon DOS between its inner and outer walls and their corresponding isolated SWCNTs. A notable phonon softening was observed in the outer wall, while a corresponding phonon hardening appeared in the inner wall. However, the low-frequency radial phonon DOS of both walls decreased compared to that of the corresponding SWCNTs. Combined with previous studies on thermal conductivity of DWCNTs,[108] this suggests that inter-wall interactions effectively suppress radial vibrations in both the inner and outer walls, analogous to the mutual interactions observed in single-walled carbon nanotube networks.[109] To further understand this effect, we compared the RBA of the inner and outer walls in three types of DWCNTs.

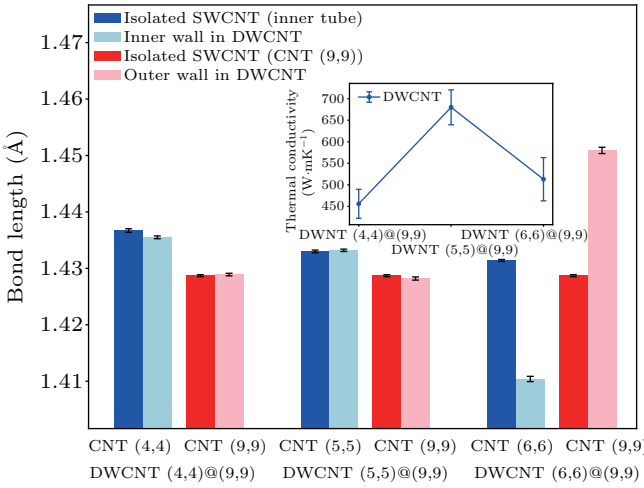


Fig. 10. Comparison of bond lengths between the inner and outer walls of three different DWCNT configurations and their corresponding isolated SWCNTs. The inset shows the thermal conductivity of the three DWCNT configurations.

As shown in supplementary Fig. S13, both the inner and outer walls of DWCNT (6,6)@(9,9) exhibit stronger suppression of vibrational amplitudes. We attribute this observation to enhanced van der Waals inter-wall interactions in DWCNTs, which increase phonon–phonon scattering and suppress radial vibrations. These effects reduce the thermal conductivity of DWCNTs. Moreover, a recent study by Sun *et al.*[110] discussed strongly hybridized phonon modes in DWCNTs, which arise from the degenerate coupling of transverse acoustic modes between the inner and outer tubes. Additionally, supplementary Figs. S11 and S12 show that the inner and outer walls of DWCNTs exhibit more phonon peaks compared to their single-walled counterparts, due to interlayer interactions that cause resonant coupling of atomic vibrations and lead to mode hybridization. These hybridized modes are distinct from the vibrational modes of isolated nanotubes, as they arise from correlated vibrations between the inner and outer walls, leading to additional peaks in the phonon density of states. It should be emphasized that the total number of vibrational modes remains unchanged. Instead, modes that originally existed separately in the individual tubes become coupled and can simultaneously appear on both the inner and outer walls. Therefore, a comprehensive investigation of DWCNTs' thermal conductivity must consider these modes and their coupling effects on heat transport.

4. Conclusion

In this study, we employed the ReaxFF-*nn* MLP combined with NEMD simulations to calculate the thermal conductivity of various carbon materials. For graphene and SWCNTs, we revisited the length dependence of their thermal conductivity. The simulation results showed that the average phonon MFP of graphene is 415.3 nm with a diffusive thermal conductivity of 2045.8 $\mathrm{W\cdot m^{-1}\cdot K^{-1}}$. Although CNTs have a lower average phonon MFP and diffusive-limit thermal conductivity than graphene, their average relaxon MFP effectively indicates that heat carriers can propagate longer distances. We focused on the relationship between the thermal conductivity of SWCNTs and their diameters. Our analysis revealed that the thermal conductivity of SWCNTs is lower than that of graphene but gradually approaches it as the tube diameter increases. Analyses of bond length and phonon DOS revealed that rolling graphene into CNTs introduces tensile strain, which decreases with increasing tube diameter; correspondingly, RBA decreases with increasing bond length. DWCNT (6,6)@(9,9), with the smallest interwall spacing, showed the lowest thermal conductivity due to enhanced van der Waals interactions that cause pronounced strain and a marked reduction in RBA. This study offers insights into CNTs and van der Waals materials formed by their assemblies.

Data availability statement

The potential model and example codes to reproduce the data of this manuscript are freely available at GitHub.

Acknowledgment

Project supported by the National Natural Science Foundation of China (Grant Nos. 11504153 and 12002325).

References

[1] Kelly M J 1995 *Low-Dimensional Semiconductors: Materials, Physics, Technology, Devices* Vol. 3 (Oxford : Clarendon Press)
[2] Chen J, Wang B and Hu Y 2017 *J. Mech. Phys. Solids* **107** 451
[3] Cao M S, Wang X X, Zhang M, Shu J C, Cao W Q, Yang H J, Fang X Y and Yuan J 2019 *Adv. Funct. Mater.* **29** 1807398
[4] Ghosh S, Calizo I, Teweldebrhan D, Pokatilov E P, Nika D L, Balandin A A, Bao W, Miao F and Lau C N 2008 *Appl. Phys. Lett.* **92**
[5] Balandin A A, Ghosh S, Bao W, Calizo I, Teweldebrhan D, Miao F and Lau C N 2008 *Nano Lett.* **8** 902
[6] Malekpour H and Balandin A A 2018 *J. Raman Spectrosc.* **49** 106
[7] Agrawal A and Choudhary A 2016 *APL Mater.* **4** 053208
[8] LeCun Y 1995 *The Handbook of Brain Theory and Neural Networks* Vol. 3361 (Cambridge : MIT Press)
[9] Behler J and Parrinello M 2007 *Phys. Rev. Lett.* **98** 146401
[10] Thompson A, Swiler L, Trott C, Foiles S and Tucker G 2015 *J. Comput. Phys.* **285** 316
[11] Shapeev A V 2016 *Multiscale Model. Simul.* **14** 1153
[12] Wang H, Zhang L, Han J and Weinan E 2018 *Comput. Phys. Commun.* **228** 178
[13] Drautz R 2019 *Phys. Rev. B* **100** 249901
[14] Ye Z H, Liu J H, Chai C G, Wen Y S, Cui S X, Zhang G Q, Li K J, Guo F and Wang X C 2025 *Phys. Chem. Chem. Phys.* **27** 10571
[15] Fan Z, Zeng Z, Zhang C, Wang Y, Song K, Dong H, Chen Y and Ala-Nissila T 2021 *Phys. Rev. B* **104** 104309
[16] Schulz E, Speekenbrink M and Krause A 2018 *J. Math. Psychol.* **85** 1
[17] Noé F 2020 *Machine Learning Meets Quantum Physics* pp. 331 (Springer)
[18] Xie S R, Rupp M and Hennig R G 2023 *npj Comput. Mater.* **9** 162
[19] Kartamyshev A, Lipnitskii A, Chepelev I, Vyazmin A and Poletaev D 2024 *Comput. Mater. Sci.* **242** 113100
[20] Hu J, Zuo Y, Hao Y, Shu G, Wang Y, Feng M, Li X, Wang X, Sun J, Ding X, Gao Z, Zhu G and Li B 2023 *Chin. Phys. B* **32** 046301
[21] Li Z, Li M, Luo Y, Cao H, Liu H and Fang Y 2025 *Digital Discovery* **4** 204
[22] Novoselov K S, Geim A K, Morozov S V, Jiang D E, Zhang Y, Dubonos S V, Grigorieva I V and Firsov A A 2004 *Science* **306** 666
[23] Avouris P and Dimitrakopoulos C 2012 *Mater. Today* **15** 86
[24] Balandin A A 2011 *Nat. Mater.* **10** 569
[25] Hu J, Ruan X and Chen Y P 2009 *Nano Lett.* **9** 2730
[26] Berber S, Kwon Y K and Tománek D 2000 *Phys. Rev. Lett.* **84** 4613
[27] Li P, Feng D, Feng Y, Liu X, Xiong M, Zhang X and Liu J 2022 *J. Therm. Sci.* **31** 1016
[28] Zhao H B, Tang D M, Zhang L, Zou M K, Xie R H, Liu C and Cheng H M 2025 *J. Mater. Sci. Technol.* **221** 46
[29] Kumanek B and Janas D 2019 *J. Mater. Sci.* **54** 7397
[30] Pop E, Mann D, Wang Q, Goodson K and Dai H 2006 *Nano Lett.* **6** 96
[31] Cao J, Yan X, Xiao Y and Ding J 2004 *Phys. Rev. B* **69** 073407
[32] Kim P, Shi L, Majumdar A and McEuen P L 2001 *Phys. Rev. Lett.* **87** 215502
[33] Wang J and Wang J S 2006 *Appl. Phys. Lett.* **88** 111909
[34] Lindsay L, Broido D and Mingo N 2009 *Phys. Rev. B* **80** 125407
[35] Maruyama S 2002 *Physica B* **323** 193
[36] Zhang G and Li B 2005 *J. Chem. Phys.* **123** 114714
[37] Zhang G and Li B 2005 *J. Chem. Phys.* **123** 014705
[38] Lukes J R and Zhong H 2007 *J. Heat Transf.* **129** 705
[39] Bruns D, Nojeh A, Phani A S and Rottler J 2020 *Phys. Rev. B* **101** 195408
[40] Liu K, Hong X, Wu M, Xiao F, Wang W, Bai X, Ager J W, Aloni S, Zettl A, Wang E and Wang F 2013 *Nat. Commun.* **4** 1375
[41] Gordeev G, Wasserroth S, Li H, Flavel B and Reich S 2021 *Nano Lett.* **21** 6732
[42] Xue L Y, Guo F, Wen Y S, Feng S Q, Huang X N, Guo L, Li H S, Cui S X, Zhang G Q and Wang Q L 2021 *Phys. Chem. Chem. Phys.* **23** 19457
[43] Plimpton S 1995 *J. Comput. Phys.* **117** 1
[44] Thompson A P, Aktulga H M, Berger R, Bolintineanu D S, Brown W M, Crozier P S, in 't Veld P J, Kohlmeyer A, Moore S G, Nguyen T D, Shan R, Stevens M J, Tranchida J, Trott C and Plimpton S J 2022 *Comput. Phys. Commun.* **271** 108171
[45] Nosé S 1984 *J. Chem. Phys.* **81** 511
[46] Hoover W G 1985 *Phys. Rev. A* **31** 1695
[47] Chen J, Zhang G and Li B 2010 *J. Phys. Soc. Jpn.* **79** 074604
[48] Stukowski A 2009 *Model. Simul. Mater. Sci. Eng.* **18** 015012
[49] Osman M A and Srivastava D 2001 *Nanotechnology* **12** 21
[50] Ozsipahi M, Jean S, Beskok A and Wilson A A 2025 *Int. Commun. Heat Mass Transf.* **163** 108658
[51] Rahman M H, Chowdhury E H, Bin Shahadat M R and Islam M M 2021 *Comput. Mater. Sci.* **191** 110338
[52] Dias F S and Machado W S 2018 *Comput. Condens. Matter* **15** 21
[53] Soler J M, Artacho E, Gale J D, García A, Junquera J, Ordejón P and Sánchez-Portal D 2002 *J. Phys.: Condens. Matter* **14** 2745
[54] Togo A and Tanaka I 2015 *Scr. Mater.* **108** 1
[55] Tadano T, Gohda Y and Tsuneyuki S 2014 *J. Phys.: Condens. Matter* **26** 225402
[56] Zhang J, Huang X, Yue Y, Wang J and Wang X 2011 *Phys. Rev. B* **84** 235416
[57] Porter L J, Li J and Yip S 1997 *J. Nucl. Mater.* **246** 53
[58] Wen Y, Xue X, Zhou X, Guo F, Long X, Zhou Y, Li H and Zhang C 2013 *J. Phys. Chem. C* **117** 24368
[59] Huang X, Guo F, Yao K, Lu Z, Ma Y, Wen Y, Dai X, Li M and Long X 2020 *Phys. Chem. Chem. Phys.* **22** 11956
[60] Bu Y, Guo F, Li K, Liang Z, Zhang J, Jiang C and Bi Z 2022 *Appl. Surf. Sci.* **593** 153451
[61] Diao C, Dong Y and Lin J 2017 *Int. J. Heat Mass Transf.* **112** 903

[62] van Duin A C, Dasgupta S, Lorant F and Goddard W A 2001 *J. Phys. Chem. A* **105** 9396

[63] Guo F, Wen Y S, Feng S Q, Li X D, Li H S, Cui S X, Zhang Z R, Hu H Q, Zhang G Q and Cheng X L 2020 *Comput. Mater. Sci.* **172** 109393

[64] Stuart S J, Tutein A B and Harrison J A 2000 *J. Chem. Phys.* **112** 6472

[65] Lindsay L and Broido D A 2010 *Phys. Rev. B* **81** 205441

[66] Rowe P, Deringer V L, Gasparotto P, Csányi G and Michaelides A 2020 *J. Chem. Phys.* **153** 034702

[67] Balandin A and Wang K L 1998 *Phys. Rev. B* **58** 1544

[68] Wang J, Li C, Sheng Y, Su Y and Yang L 2022 *Appl. Phys. Lett.* **121** 042202

[69] Bae M H, Li Z, Aksamija Z, Martin P N, Xiong F, Ong Z Y, Knezevic I and Pop E 2013 *Nat. Commun.* **4** 1734

[70] Klemens P 1951 *Proc. R. Soc. A* **208** 108

[71] Cepellotti A and Marzari N 2016 *Phys. Rev. X* **6** 041013

[72] Fugallo G, Cepellotti A, Paulatto L, Lazzeri M, Marzari N and Mauri F 2014 *Nano Lett.* **14** 6109

[73] Cao A and Qu J 2012 *J. Appl. Phys.* **112** 013503

[74] Xu X, Pereira L F C, Wang Y, Wu J, Zhang K, Zhao X, Bae S, Tinh Bui C, Xie R, Thong J T L, Hong B H, Loh K P, Donadio D, Li B and Özyilmaz B 2014 *Nat. Commun.* **5** 3689

[75] Thomas J A, Iutzi R M and McGaughey A J 2010 *Phys. Rev. B* **81** 045413

[76] Pan R Q, Xu Z J and Zhu Z Y 2007 *Chin. Phys. Lett.* **24** 1321

[77] Park M, Lee S C and Kim Y S 2013 *J. Appl. Phys.* **114** 053506

[78] Cai W, Moore A L, Zhu Y, Li X, Chen S, Shi L and Ruoff R S 2010 *Nano Lett.* **10** 1645

[79] Savin A V, Hu B and Kivshar Y S 2009 *Phys. Rev. B* **80** 195423

[80] Tersoff J 1989 *Phys. Rev. B* **39** 5566

[81] Brenner D W 1990 *Phys. Rev. B* **42** 9458

[82] Si C, Wang X D, Fan Z, Feng Z H and Cao B Y 2017 *Int. J. Heat Mass Transf.* **107** 450

[83] Huang L, Joshi K L, van Duin A C T, Bandosz T J and Gubbins K E 2012 *Phys. Chem. Chem. Phys.* **14** 11327

[84] Hone J, Whitney M and Zettl A 1999 *Synth. Met.* **103** 2498

[85] Yoshino K, Kato T, Saito Y, Shitaba J, Hanashima T, Nagano K, Chiashi S and Homma Y 2018 *ACS Omega* **3** 4352

[86] Feng Y, Sato Y, Inoue T, Xiang R, Suenaga K and Maruyama S 2023 *Small* **20** 2308571

[87] Zhou G, Cen C, Wang S, Deng M and Prezhdo O V 2019 *J. Phys. Chem. Lett.* **10** 7179

[88] Jensen S A, Ulbricht R, Narita A, Feng X, Müllen K, Hertel T, Turchinovich D and Bonn M 2013 *Nano Lett.* **13** 5925

[89] Liang S, Zheng L J, Song L N, Wang X X, Tu W B and Xu J J 2024 *Adv. Mater.* **36** 2307790

[90] Lindsay L, Broido D A and Mingo N 2010 *Phys. Rev. B* **82** 161402

[91] Li P, Feng D, Feng Y, Liu X, Xiong M, Zhang X and Liu J 2022 *J. Therm. Sci.* **31** 1016

[92] Dorgan V E, Behnam A, Conley H J, Bolotin K I and Pop E 2013 *Nano Lett.* **13** 4581

[93] Li Q, Liu C, Wang X and Fan S 2009 *Nanotechnology* **20** 145702

[94] Pop E, Mann D, Cao J, Wang Q, Goodson K and Dai H 2005 *Phys. Rev. Lett.* **95** 155505

[95] Yu C, Shi L, Yao Z, Li D and Majumdar A 2005 *Nano Lett.* **5** 1842

[96] Kodama T, Ohnishi M, Park W, Shiga T, Park J, Shimada T, Shinohara H, Shiomi J and Goodson K E 2017 *Nat. Mater.* **16** 892

[97] Parrish K D, Jain A, Larkin J M, Saidi W A and McGaughey A J 2014 *Phys. Rev. B* **90** 235201

[98] Xiao X and Yuan C 2024 *Appl. Phys. Lett.* **125**

[99] Qiu B, Wang Y, Zhao Q and Ruan X 2012 *Int. Conf. Micro/Nanoscale Heat Transfer* (American Society of Mechanical Engineers) pp. 633–638

[100] Szczygielska A, Jabłońska A, Burian A, Dore J C, Honkimaki V and Nagy J B 2000 *Acta Phys. Pol. A* **98** 611

[101] Klemens P and Pedraza D 1994 *Carbon* **32** 735

[102] Zhang J and Zuo J 2009 *Carbon* **47** 3515

[103] Zhou Y, Dong Z Y, Hsieh W P, Goncharov A F and Chen X J 2022 *Nat. Rev. Phys.* **4** 319

[104] Kumar A, Abhikeern K and Singh A 2025 *J. Appl. Phys.* **137** 134302

[105] Qin Y, Zong Z, Che J, Li T, Fang H and Yang N 2025 *Appl. Phys. Lett.* **126** 104101

[106] Thomas J A, Turney J E, Iutzi R M, Amon C H and McGaughey A J H 2010 *Phys. Rev. B* **81** 081411

[107] Zhang H, Wang L and Wang J 2007 *Comput. Mater. Sci.* **39** 664

[108] Zhang X, Zhou W X, Chen X K, Liu Y Y and Chen K Q 2016 *Phys. Lett. A* **380** 1861

[109] Yin H, Liu Z and Yang J 2023 *Chin. Phys. B* **32** 044401

[110] Sun S, Lin Q, Li Y, Kozawa D, Wu H, Maruyama S, Moon P, Kariyado T, Kitaura R and Zhao S 2025 *Phys. Rev. Lett.* **134** 176101